'Dial up' Photonic Integrated Circuit Filter

Xumeng Liu , Guanghui Ren , *Senior Member, IEEE*, Xingyuan Xu, Aditya Dubey, Timothy Feleppa, Andreas Boes, Arnan Mitchell , *Senior Member, IEEE*, and Arthur Lowery

Abstract—Photonic integrated circuits (PICs) are capable of providing advanced signal processing functions in small footprints; however, their operation is affected by fabrication tolerances in addition to dynamically changing thermal and acoustic effects. Thus, it can be difficult to tune PICs to accurately implement desired functionality, even those with a relatively small number of photonic components (e.g. 10). In this contribution, we demonstrate a 'dial-up' PIC filter that can accurately and reliably implement a wide range of filter functions. It uses an on-chip optical reference path, which allows the phase and amplitude of each tap in a finite impulse response (FIR) filter to be individually determined. The fractional delay of the reference path is chosen to be half the delay between the FIR filter's taps, which upon Fourier transformation enables us to uniquely identify the phase and amplitude of each tap in the FIR filter. This information is used in an independent feedback algorithm to control each tap to ensure that a desired ('dialed-up') response is accurately implemented. To demonstrate the flexibility of the method, we experimentally demonstrate functions of a sinc-shaped filter with a phase step, a Hilbert transform and low- and high-pass filters.

Index Terms—Photonic integrated circuit, tunable optical filter, programmable photonics, self-calibration, phase recovery, finite-impulse-response filter, optical Hilbert transform.

I. INTRODUCTION

PHOTONIC integrated circuits (PICs), which are capable of manipulating the flow of light on a chip scale, can be used for a variety of applications such as optical fiber communications [1], [2], quantum information processing [3], [4], neuromorphic computing [5], [6], [7] and artificial intelligence [8], [9]. In contrast to conventional electronic integrated circuits, photonic circuit technology has advantages in

Xumeng Liu, Timothy Feleppa, and Arthur Lowery are with the Electro-Photonics Laboratory, Department of Electrical and Computer Systems Engineering, Monash University, Clayton, VIC 3800, Australia (e-mail: xumeng.liu@monash.edu; timothy.feleppa@monash.edu; Arthur.lowery@ monash.edu).

Guanghui Ren, Aditya Dubey, and Arnan Mitchell are with the Integrated Photonics and Applications Centre, School of Engineering, RMIT University, Melbourne, VIC 3000, Australia (e-mail: guanghui.ren@rmit.edu.au; s3762140@student.rmit.edu.au; arnan.mitchell@rmit.edu.au).

Xingyuan Xu is with the State Key Laboratory of Information Photonics and Optical Communications, Beijing University of Posts and Telecommunications, Beijing 100876, China (e-mail: xingyuanxu@bupt.edu.cn).

Andreas Boes is with the Institute for Photonics and Advanced Sensing (IPAS), School of Electrical and Electronic Engineering, University of Adelaide, Adelaide, SA 5005, Australia (e-mail: andy.boes@adelaide.edu.au).

terms of terahertz processing bandwidths for a moderate power consumption. Application-specific photonic integrated circuits (ASPICs) can be designed and manufactured using standardized building blocks, which when assembled as a circuit give a fixed response [10], [11], [12]. Programmable PICs offer more flexibility, in that they can be reprogrammed once deployed to form dynamic elements in optical networks, such as wavelength selective switches and wavelength routers [13], [14]. Moreover, recent advances in PIC technology support complex topologies in various waveguide platforms [15], [16], [17].

Although programmable PICs are very powerful, their operation is sensitive to manufacturing tolerances, acoustic vibrations and thermal variation including crosstalk between the phase-control elements [18], [19]. Thus, it can be challenging to implement a desired processing function accurately in a programmable PIC and maintain it, while in other applications it may be critical to dynamically change filtering functionality, such as for optical equalization of dynamic variations in fiber-optic transmission channels [20].

To mitigate the effect of fabrication tolerances and minimize thermal crosstalk and environmental perturbation, control techniques are required to implement a desired PIC function accurately and reliably. With such control, a desired function could be 'dialed up' automatically, increasing the practicality of programmable PICs in, say, optical communications systems [21], [22], [23], [24]. An alternative would be to use a look-up table to set the control elements on the chip, but this would rely on the characteristics of the PIC being stable with respect to its control parameters, so would require a stable operating environment and full knowledge of the thermal crosstalk, if heaters were used to control the phase elements.

For the control systems to work, they require observable information, such as the frequency response of the filter including its phase response. Although the intensity response is easy to measure, using a tuneable laser and a photodiode for example, optical phase is problematic as it requires a reference path, which is usually external to the PIC and subject to thermal and acoustic variations [21], [22], [23], [24]. Thus, novel self-calibration methods that only rely on detecting intensity have been proposed, in which the phase information of the signal processing core is extracted from the intensity information using an on-chip reference path. In our previous demonstration, we used the Kramers-Kronig (KK) relationship to extract phase from intensity [25]; this relationship is valid when its minimum phase condition is satisfied, requiring that the majority of input power is used for the reference path. To overcome this and simplify the readout method, we then proposed an alternative method that

uses a Fourier transform of the intensity response of the system including the reference path; if the differential delay between the reference path and the signal-processing core's paths is one half of the delay between the signal processing core's paths, the phases of the signal-processing cores paths can be uniquely identified at the output of the Fourier transform [26]. We call this the "fractional delay reference method". This method is available for diverse filters with a discrete impulse response, such as FIR filters, infinite impulse response (IIR) filters, or some highly-meshed networks. One advantage over the KK method is that far less power is required in the reference path, so the chip has a lower loss to the signal paths. As with the KK method, only one photodetector is needed to individually determine the phases and amplitudes of each tap of the FIR filter. To date, the fractional delay reference method has not been demonstrated as part of a feedback control mechanism for the entire signal processing core; such a mechanism would enable reconfigurable 'dial-up' functionality in deployed PICs.

In this paper, we demonstrated a 'dial-up' PIC filter for the first time by employing the fractional delay reference method within a feedback control system and investigated the method's flexibility and accuracy. To demonstrate its effectiveness, we controlled a 4-tap FIR signal processing core to 'dial up' multiple signal processing functions. The control system is particularly simple, because the fractional delay reference method can determine the amplitudes and phases of the taps individually; this enables separate independent feedback loops to be used for each tap. No accurate prior knowledge of the chip's tuning characteristics, such as the phase offsets of its Mach-Zehnder tunable couplers and phase shifters, its electrode resistances or the electrical powers required for 2π phase shift of each tunable coupler, is required. We show that the algorithm-based component characterization using the fractional delay reference method matches a direct measurement within 3%. Thus, the fractional delay reference method is a promising solution to address manufacturing variations from chip to chip and environment perturbations, and make the wider adoption of programmable PICs feasible. We used the silicon nitride loaded thin-film lithium niobate (Si_3N_4/LNOI) platform as an example. The fractional delay reference method is applicable to other PIC platforms that have some form of amplitude and phase control of their paths, and support delays.

This paper is organized as follows: Section II introduces the theory of the fractional delay reference method, Section III presents the reconfigurable PIC layout, Section IV describes the control algorithm for filter taps, Section V shows the experimental setup, Sections VI and VII present the results of component characterization and self-tuning, and in Section VIII we conclude our findings.

II. THEORY OF THE FRACTIONAL DELAY REFERENCE METHOD

The idea of using a half delay for the reference path was inspired by the frequency allocation of subcarriers in optical orthogonal frequency division multiplexing (OFDM) systems. If conventional radio OFDM is transmitted over an optical channel without bias, then its negative excursions are removed because there are no negative intensities in optical channels; this clipping creates strong intermodulation distortion. A solution is to use only the odd-valued subcarriers on a frequency grid (in relation to a reference carrier) [27], because the intermodulation of subcarriers falls only on the even subcarriers, which can be rejected by the Fourier transform at the receivers. If we transform *frequency* in OFDM to *delay* in our PIC filters, then we should only use delays between our FIR taps that are twice the delay between the reference and the first tap. We can then use a Fourier transform of the power-spectrum to find the amplitudes and phases (related to the delays) of the taps, as we shall show. As with optical OFDM, the power in the reference arm should be similar to the sum of the powers in the signal processing core's taps, but without the requirement of being greater as with KK.

For the mathematical analysis, we consider a 4-tap FIR filter as the signal processing core. The FIR filter has a time delay difference of $(2n-1)\Delta T$ from the reference path for the nth tap. That is, the delay between the reference and the first FIR tap is half the duration of the incremental delays between the taps.

Consider the optical fields out of a 4-tap FIR filter and reference path, which for a CW input at angular frequency ω comprises the sum of weighted sinusoids

$$E(t,\omega) = E_{\text{ref},0} \cos(\omega t)$$
$$+ \sum_{n=1,2,3,4} E_{n,0} \cos(\omega(t-\tau_n) + \theta_n), \quad (1)$$

where $E_{\text{ref},0}$ is the amplitude of the reference path, $E_{n,0}$ are the amplitudes of the taps, τ_n are the delay values of paths n, θ_n are the phases of the taps. This can be thought of as a summation of vectors whose relative angles depend on the time delays and the CW frequency.

A typical measurement is to sweep ω over a range of values and measure the power response of the system, $P(\omega)$ which is the modulus-squared of the vector sum averaged over at least one (or any higher integer) complete period of ω, so that $T = 2\pi/\omega$ and

$$P(\omega) = \frac{1}{T} \int_0^T |E(t.\omega)|^2 \, dt. \quad (2)$$

Evaluating the modulus-squared gives

$$|E(t.\omega)|^2$$

$$= \left| E_{\text{ref},0} \cos(\omega t) + \sum_{n=1,2,3,4} E_{n,0} \cos(\omega(t-\tau_n) + \theta_n) \right|^2$$

$$= [E_{\text{ref},0} \cos(\omega t)]^2 + \sum_{n=1,2,3,4} [E_{n,0} \cos(\omega(t-\tau_n) + \theta_n)]^2$$

$$+ 2E_{\text{ref},0} \cos(\omega t) \sum_{n=1,2,3,4} E_{n,0} \cos(\omega(t-\tau_n) + \theta_n)$$

$$+ \text{cross terms between different FIR taps.} \quad (3)$$

The interference terms are explained as following:

1) The first two terms will fall at zero delay, which is corresponding to the self-mixing of the main carrier and of each subcarrier as the DC terms in OFDM systems.

2) The interference terms of the reference and a given FIR tap, which corresponds to the mixing of the main carrier and a subcarrier in OFDM, can be expressed as

$$M_n(t) = 2E_{\text{ref},0} \cos(\omega t) E_{n,0} \cos(\omega(t - \tau_n) + \theta_n)$$
$$= E_{\text{ref},0} E_{n,0} [\cos(-\omega \tau_n + \theta_n) + \cos(2\omega t - \omega \tau_n + \theta_n)]. \quad (4)$$

The $2\omega t$ terms are too high to become electrical signals upon photodetection, but the low-frequency (LF) parts remain

$$M_n(t)|_{\text{LF}} = E_{\text{ref},0} E_{n,0} \cos(-\omega \tau_n + \theta_n). \quad (5)$$

The amplitude and phase can be recovered via an inverse Fourier integral over two free spectral ranges (FSRs) of the FIR filter, which is defined as $\text{FSR} = 1/(2\Delta T)$.

$$Re[E(\tau_n)]$$
$$= k \int_{2\text{FSR}} E_{\text{ref},0} E_{n,0} \cos(-\omega \tau_n + \theta_n) \cos(\omega \tau_n) \, d\omega$$
$$= k \int_{2\text{FSR}} E_{\text{ref},0} E_{n,0} \frac{\cos(\theta_n) + \cos(-2\omega \tau_n + \theta_n)}{2} \, d\omega, \quad (6)$$

$$Im[E(\tau_n)]$$
$$= k \int_{2\text{FSR}} E_{\text{ref},0} E_{n,0} \cos(-\omega \tau_n + \theta_n) \sin(\omega \tau_n) \, d\omega$$
$$= k \int_{2\text{FSR}} E_{\text{ref},0} E_{n,0} \frac{\sin(\theta_n) - \sin(-2\omega \tau_n + \theta_n)}{2} \, d\omega, \quad (7)$$

where k is a constant that depends on the definition of the transform.

Upon integration the high-frequency terms disappear to reveal

$$Re[E(\tau_n)] = k_1 E_{\text{ref},0} E_{n,0} \cos(\theta_n), \quad (8)$$
$$Im[E(\tau_n)] = k_1 E_{\text{ref},0} E_{n,0} \sin(\theta_n), \quad (9)$$

where $k_1 = k/2$. It can be seen that these provide the phases and amplitudes of each tap independently, and this information can be used in control algorithm to independent control each tap.

(3) The cross terms of different FIR taps, which correspond to subcarrier mixing in OFDM, evaluate as

$$C(n, m) = 2E_{n,0} \cos(\omega(t - \tau_n) + \theta_n)$$
$$\times E_{m,0} \cos(\omega(t - \tau_m) + \theta_m)|_{m \neq n}$$
$$= E_{n,0} E_{m,0} [\cos(\omega(-\tau_n + \tau_m) + (\theta_n - \theta_m))$$
$$+ \cos(2\omega t + \omega(-\tau_n - \tau_m) + (\theta_n + \theta_m))]. \quad (10)$$

The second cos term has a fast oscillation and thus averages out to zero on photodetection, leaving

$$C(n, m) = E_{n,0} E_{m,0} \cos(\omega(-\tau_n + \tau_m) + (\theta_n - \theta_m)). \quad (11)$$

As the delay values of the FIR taps are odd multiples of ΔT, then their differences must be even multiples of ΔT. Thus, the cross terms fall at different delays to the delays of the FIR taps. Therefore, they can be selected and then discarded by the Fourier transform.

III. CHIP DESIGN AND FABRICATION

The design of our PIC chip is based on the fractional delay reference method theory. The architecture of the full chip is a tap-delay-line (TDL) FIR filter with a half-delay reference path to perform (1). It comprises: an array of tunable 2×2 Mach-Zehnder interferometers (MZIs) with equal arm lengths loaded with a heater on one arm to tune the power splitting ratio; an array of S-shaped spiral delay lines with a delay time of $(2n - 1)\Delta T$ between the nth tap and the reference arm; tunable phase shifters equipped on each tap except the reference arm; and an array of 3-dB directional couplers to combine/interfere the different taps.

The chip layout, shown in the optical microscope image presented in Fig. 1(b), was designed by using IPKISS photonic design framework. A series of concentric spirals with a minimum bend radius of 150 μm were used for the delay lines, and the components were organized in a compact structure to minimize the footprint. The length difference between delay lines on the neighboring tap is 4801 μm, and thus the free spectral range of the 4-tap FIR filter is 28 GHz as $2\Delta T = 35$ ps, which is designed to operate for the conventional optical communication systems with transmitting 28-Gbd signal. Moreover, the circuit topology has several additional inputs and outputs to allow access to different circuit sections independently; and it also has test inputs and outputs for coupling power ratio test. The inputs and outputs were folded into one column for optical interface packaging by using an optical fiber array; however, an advantage of the fractional delay method is that these outputs are not required to characterize or control the PIC.

The photonic integrated chip was fabricated on the silicon nitride loaded thin-film lithium niobate (Si_3N_4/LNOI) platform [26], [28], [29]. The waveguide propagation loss was measured to be 0.3 dB/cm. Grating couplers were used to interface the PIC to optical fibers [28], [30]. All the waveguide components and grating couplers were designed to work for TE mode. The titanium heaters for each tuning element were deposited on top of the waveguide and a 1-μm SiO_2 isolation layer, and each heater has a resistance of approximately 125 Ω.

The chip was packaged by connecting the heaters to a printed electrical circuit board using wire-bonding. The current to the heaters was controlled by connecting the circuit board to a programmable multi-channel power supply. The optical I/Os were pigtailed with a polarization-maintaining fiber array. The photonic circuit chip was mounted on a metal block with a Peltier module underneath to control the chip's temperature.

IV. EXPERIMENTAL SETUP

Fig. 2(a) shows the experimental setup. A tunable laser (in a LUNA OVA 5000 Optical Vector Analyzer) with an operating range from 1525.00 nm to 1611.19 nm and a scanning step of 0.0012 nm, was followed by a C+L band EDFA (FiberLabs
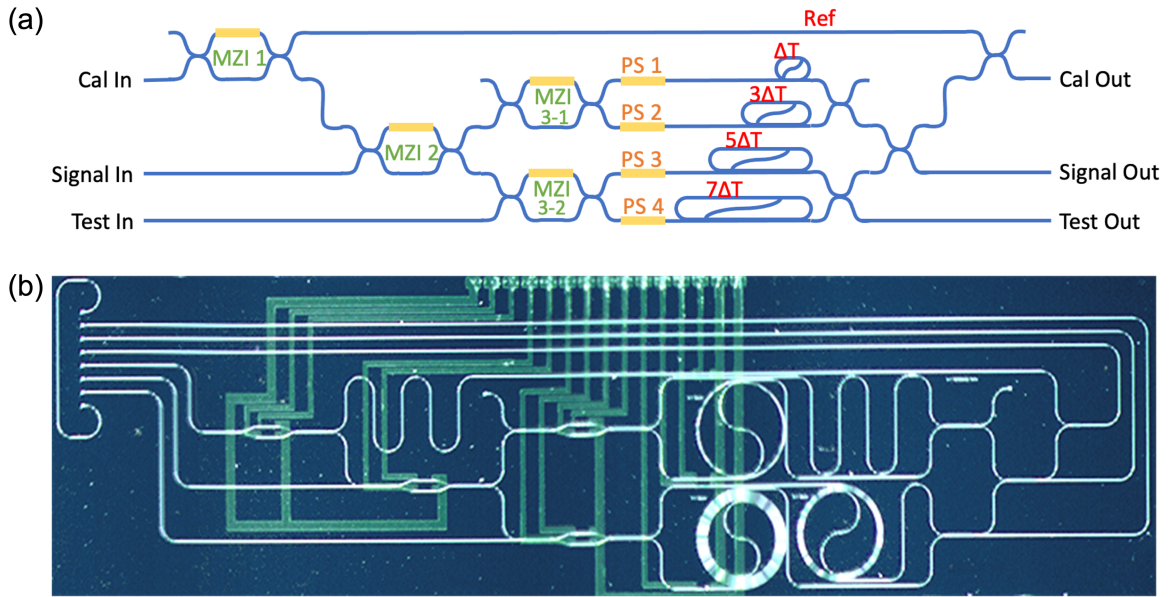
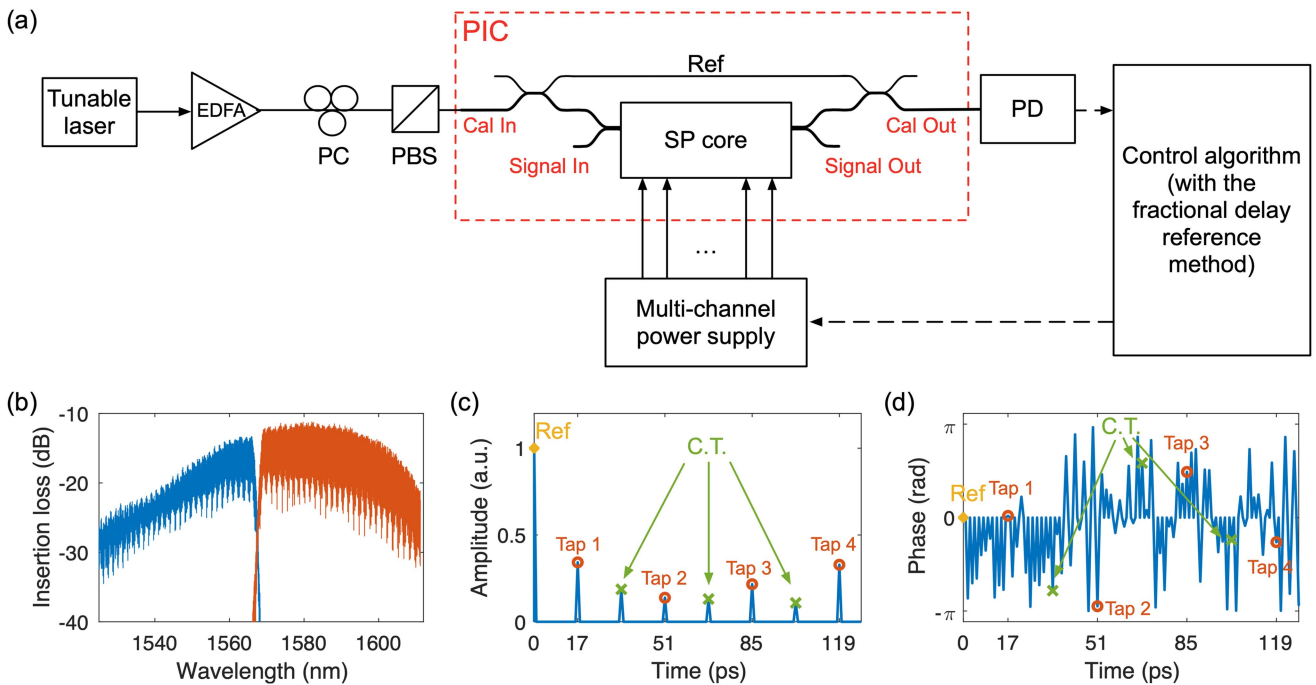Fig. 1. (a) Schematic and (b) microscope image of the 4-tap FIR filter with a half-tap delayed reference path.

Fig. 2. (a) Experimental setup of the control algorithm to enable a desired response to be 'dialed up'. (b) Insertion loss spectrum measured between Cal In and Cal Out, including the reference path. (c) Amplitude and (d) phase of derived impulse response of the whole system, as appears at the output of the Fourier transform. C.T. means the cross terms (10).

AMP-FL8021-CLB) to compensate coupling and waveguide losses of the device. As the grating couplers on the PIC are intrinsically sensitive to polarization, a polarization controller (PC) and polarizing beam splitter (PBS) were used to ensure that only TE-polarized light is coupled into the chip. The magnitude of the optical insertion loss spectra of the chip was measured by the LUNA OVA. Obviously the long optical paths (necessary for optical amplification) suffer from large phase variations due

to thermal and vibrational effects, and so would hinder direct phase measurements of the FIR filter.

Fig. 2(b) shows the insertion loss spectrum measured between Cal In and Cal Out. The frequency response was measured over two bands (blue - C-band, orange - L-band) as the LUNA OVA switches between bands. The wide-band variation in response is dominated by the PIC's grating couplers, which performs best around 1575 nm. Fig. 2(c) and (d) show the derived impulse

response of the whole system, as appears at the output of the Fourier transform. The algorithm will discard the reference (Ref.) and the cross terms (C.T.) to obtain the response of just the signal processing core (Taps). Note that the phases appear to be random where the signal amplitudes are near zero, as the inputs to the phase calculations are dominated by noise.

V. CONTROL ALGORITHM FOR FILTER TAPS

The control system initially characterizes the tunable components and afterwards tunes the signal processing core.

Firstly, the tunable components are individually characterized, using the following steps: (1) measurement of the intensity frequency response, (2) recovery of the tap weights by the fractional delay reference method. This is repeated for a range of control voltages on each element, so that the control voltage sensitivities and bias points can be fitted to the measurements that are stored.

Secondly, to 'dial up' a desired response of the signal processing core, the self-tuning algorithm uses several steps: (3) power spectrum measurement between Cal In and Cal Out, (4) determination of the tap weights using the fractional delay reference method, (5) estimation of the tap errors compared with those that would theoretically give the desired response, (6) update of all tap weights based on resolving a fraction of the error, (7) conversion from tap weights to the electrical voltages using the stored sensitivities, (8) update voltages via a programmable power supply. The algorithm iterates towards the desired response by repeating Steps 3 to 8. Fig. 3 shows the self-tuning algorithm flowchart.

In terms of our FIR-structured signal processing core, the relationship between tap weights and component parameters are explained below. The weight for Tap n is

$$w_{n,i} = A_{n,i}e^{j\phi_{n,i}}, \qquad (12)$$

where n is the tap number, A is the amplitude of tap weight, ϕ is the phase of tap weight, and i is the iteration counter.

In terms of a phase shifter as a basic tuning element, the relationship between phase shift and the applied electrical power $P_{\text{elec},i}$ is

$$\phi_i = 2\pi \frac{P_{\text{elec},i}}{P_{2\pi}}, \qquad (13)$$

where $P_{2\pi}$ is the electrical power required for 2π phase shift.

With the above equations, we can determine the electrical power required for each tuning element by knowing the tap weights. By comparing the actual electrical power and the desired values, the errors ΔP are obtained and used to update the electrical power onto the chip,

$$P_{i+1} = P_i + \mu \Delta P_i, \qquad (14)$$

where μ is an update factor. Suitable update factors are set respectively for the update power of MZIs and phase shifters to avoid oscillation and make a slow convergence. The updated electrical power is wrapped within a reasonable range from 0 to $P_{2\pi}$. The electrical power applied to each tuning component (P_{MZI} and P_{ϕ}) is updated in each iteration.

VI. CALIBRATION FOR TUNABLE COMPONENTS

To demonstrate that a MZI can be accurately calibrated (to find its sensitivity and bias points), we used Test In and Test Out to access MZI 3-2.

The extinction ratio of MZI 3-2 can be described as

$$ER\,[dB] = 10\log_{10}\left(\frac{P_{\text{out},2}}{P_{\text{in},2}}\right)$$
$$= 10\log_{10}\left(\sin^2\left(\pi\frac{P_{\text{elec}}}{P_{2\pi}} + \frac{\phi_{\text{int}}}{2}\right)\right), \qquad (15)$$

where P_{in} and P_{out} are optical power, P_{elec} is the applied electrical power, $P_{2\pi}$ is the electrical power required for 2π phase shift, ϕ_{int} is the initial phase.

The optical power at Output 3 was measured with sweeping the applied electrical power on MZI 3-2 from 0 to 0.32 W. Fig. 4(a) shows the extinction ratio of MZI 3-2 as a function of the applied electrical power. A bias power of 0.28 W is needed to generate a phase change of 2π and the initial phase is 0.15π. The extinction ratio of MZI 3-2 was measured to be 38 dB.

To verify the viability of the component characterization algorithm, we used Cal In and Cal Out as optical I/Os to give a reference path and a 4-tap FIR filter. The insertion loss spectrum was measured by LUNA OVA 5000 while sweeping the applied electrical power of MZI 3-2, and the tap weights were recovered by the fractional delay reference method.

The power splitting ratio of a MZI can be expressed as

$$PSR\,[dB] = 10\log_{10}\left(\frac{P_{\text{out,upper}}}{P_{\text{out,lower}}}\right)$$
$$= 10\log_{10}\left(\tan^2\left(\pi\frac{P_{\text{elec}}}{P_{2\pi}} + \frac{\phi_{\text{int}}}{2}\right)\right), \qquad (16)$$

where P_{out} are optical power at the upper or lower output port, P_{elec} is the applied electrical power, $P_{2\pi}$ is the electrical power required for 2π phase shift, ϕ_{int} is the initial phase.

Fig. 4(b) shows the power splitting ratio recovered by the fractional delay reference method as a function of the applied electrical power. A bias power of 0.29 W is needed to generate a phase change of 2π and the initial phase is 0.18π. The maximum power splitting ratio of MZI 3-2 is 38 dB.

By comparing the characterization result (from the LUNA OVA) and algorithm-derived result, the variation of $P_{2\pi}$ is 3%, which is in broad agreement with the accuracy of the LUNA. This verifies the fractional delay reference method, indicating that it can be used for component calibration.

The phase and amplitude of all the taps' weights are recovered by the fractional delay reference method. Fig. 4(c) shows the optical power in each tap when tuning MZI 3-2. It can be seen that MZI 3-2 controls the intensities of Tap 3 and Tap 4. However, there exists also thermal crosstalk to Tap 1 and Tap 2. That is, the tuning of MZI 3-2 results in a 5-dB variation of Tap 1 and Tap 2.

VII. SELF-TUNING OF 4-TAP FIR FILTER

We first verified the feasibility of chip self-tuning by demonstrating diverse transfer functions, including a sinc filter with a
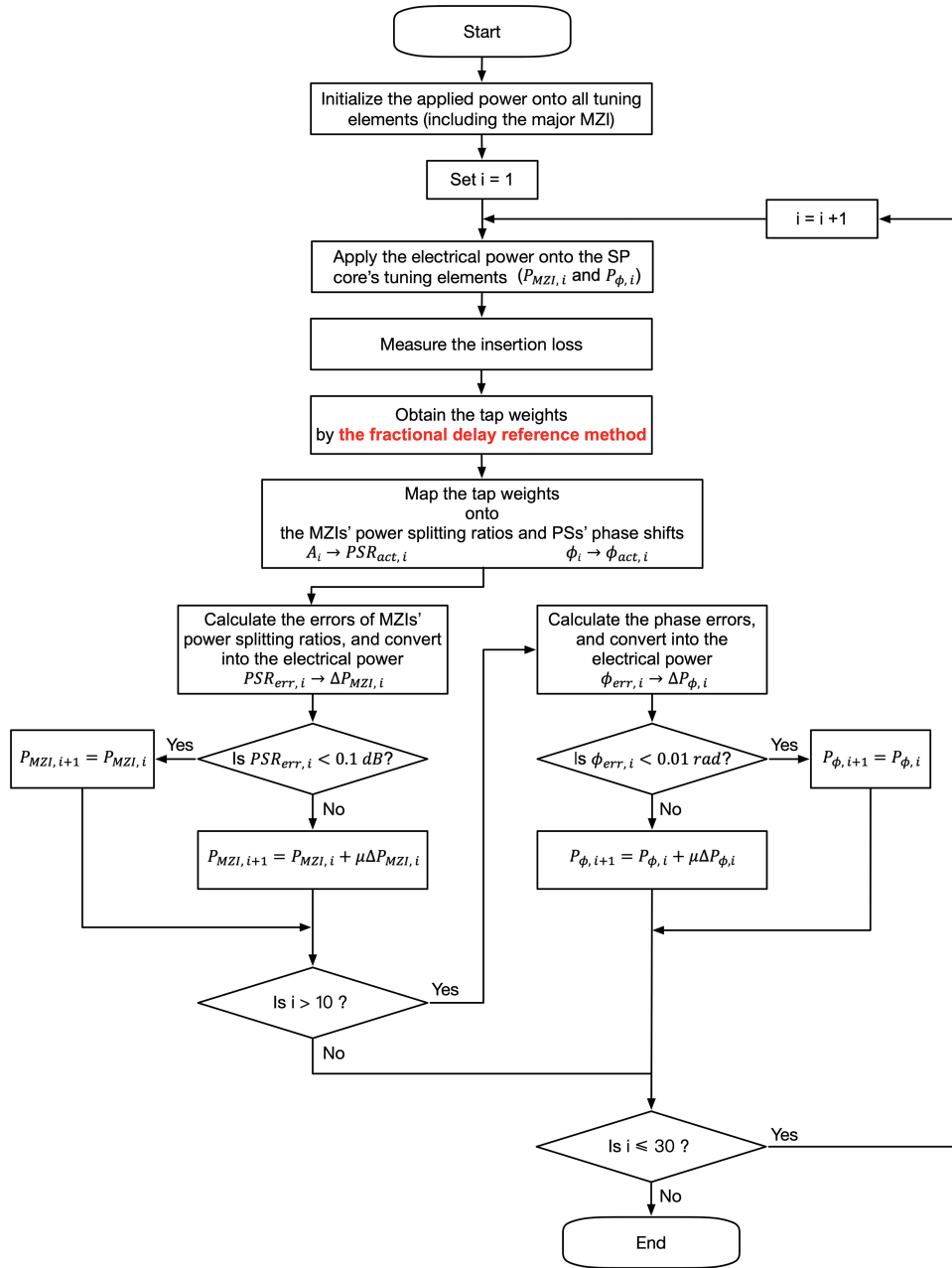
Fig. 3.   Flowchart of the self-tuning algorithm. This controller acts upon each tap independently, and so makes no use of any prior knowledge of crosstalk mechanisms. Note that this is a simple iterative controller, and there will be more sophisticated algorithms that could achieve convergence more rapidly.
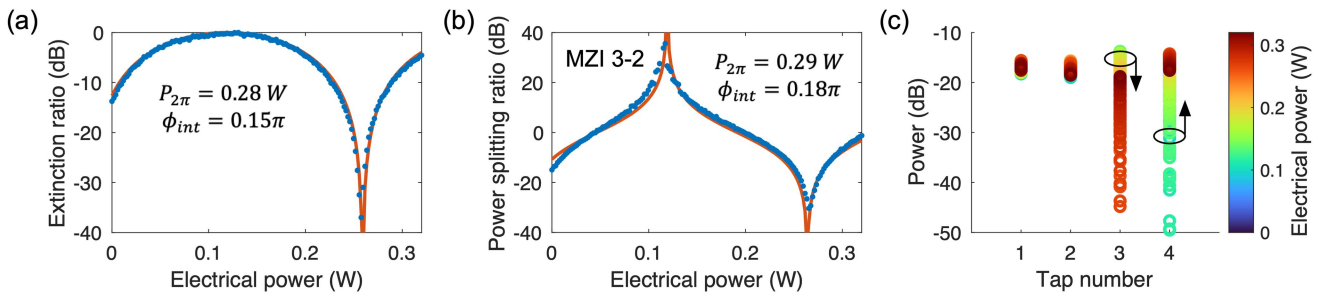

Fig. 4.   (a) Extinction ratio of MZI 3-2 measured between Test In and Test Out. (b) Power splitting ratio of MZI 3-2 determined by the algorithm for component characterization. (The measured results are shown in blue and a fitted curve is shown in red.) (c) Optical power of each tap when sweeping the electrical power of MZI 3-2.
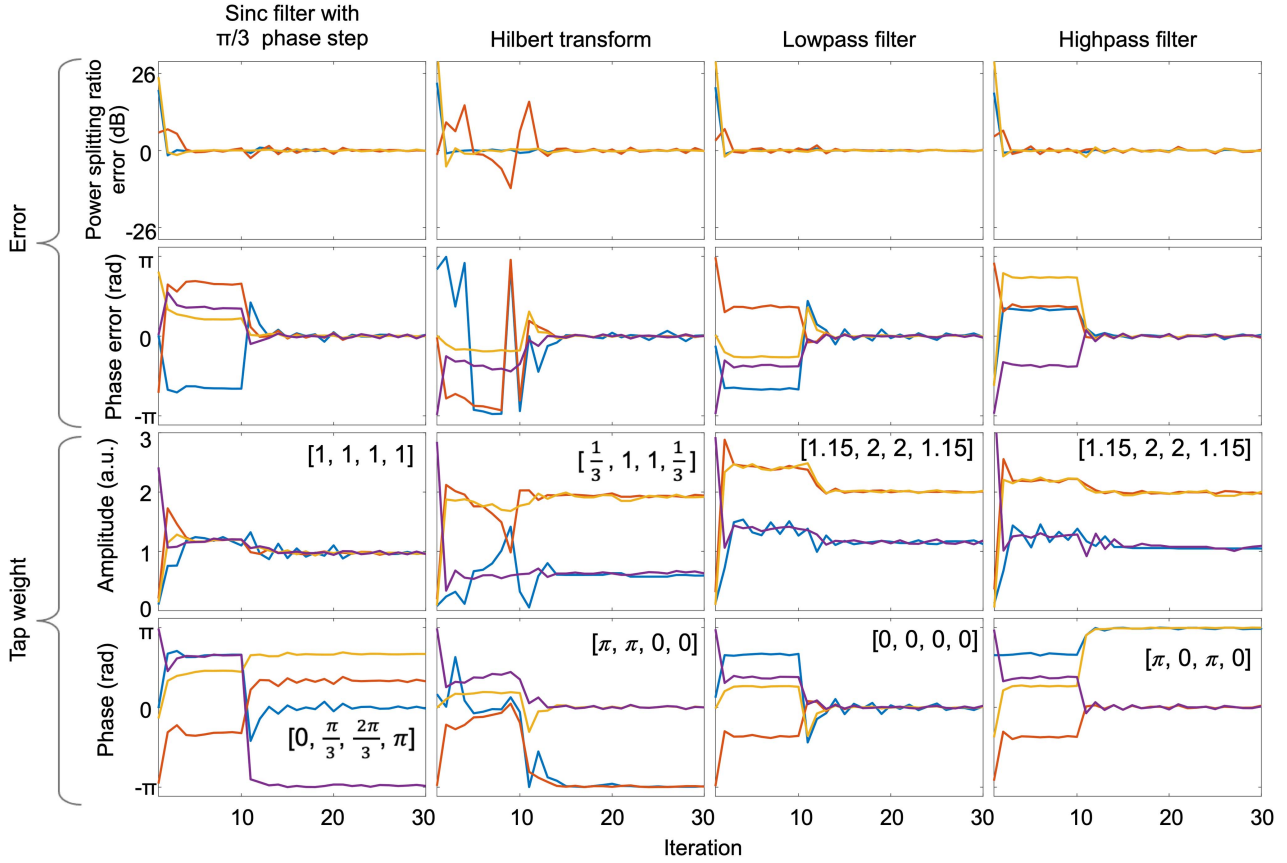
Fig. 5. The convergence of errors and tap weights during the self-tuning process for various signal-processing functions. Note that blue - Tap 1, orange - Tap 2, yellow - Tap 3, purple - Tap 4. All taps converge to near their design values for a particular function, as shown by the error plots. The design values of tap weights are also listed in the tap weights plots.

phase step, a Hilbert transformer, an inverse sinc lowpass filter, and inverse sinc highpass filter.

During the self-tuning process, the electrical power applied onto the MZI 1 (which controls the intensities of the reference path and the 4-tap FIR filter) was fixed (0.18 W) to approximately divide the swept laser's power equally between the signal processing core and the reference path. The electrical powers applied to each tunable components of the 4-tap FIR filter was initially set to compensate the initial phase and trained to perform the desired function. The free spectral range of the 4-tap FIR filter is 28 GHz, set by a 35-ps delay increment of between adjacent delay paths. Note that the FSR of the 4-tap signal processing core alone is half of the FSR when the reference path is included. That is, two FSRs of the signal processing core was measured to recover the phase from amplitude.

The electrical power needed to achieve 2π phase shifts for the MZIs and phase shifters $P_{2\pi}$ is set to be 0.32 W and 0.24 W based on the characterization results, which can be defined roughly as the errors will be eliminated during the self-tuning process. For feasibility, we allow a 0.1-dB error tolerance of power splitting ratio and a 0.01-rad phase error tolerance in Step 7 of the self-tuning algorithm.

Each iteration in Figure. 3 takes 16.5 seconds. This comprises: (a) 5-second scanning time of the tunable laser within the LUNA OVA, to measure the power response (averaged over 10 scans);

the scanning range (328.5 GHz) is larger than the calibration FSR range (56 GHz), but this is the minimum setting for the LUNA, (b) communication delays between the PC and the programmable power supply. Note that this interval allows the heaters to stabilize between iterations, and also the thermal crosstalk to settle. Some improvements can be made by speeding up the iteration rate and implementing a Proportional-Integral-Derivative (PID) control loop, although optimizing the different PID parameters might be challenging.

Fig. 5 plots the tap weights and errors as they converge. Our experiments show that the whole system converges with using the independent control loops (In Fig. 3). That is, the control system is stable even with the interactions of the taps via thermal crosstalk. The self-tuning process can be successfully completed within 30 iterations. In order to achieve a stable convergence, only half the measured amplitude errors are compensated per iteration and the phase errors are not used for update for the first 10 iterations ($\mu_{MZI} = 0.5$, $\mu_{PS} = 0$); this prevents oscillation of the tuning voltages during the amplitude and phase convergences. After 10 iterations, half the measured errors are compensated for both amplitude and phase ($\mu_{MZI} = \mu_{PS} = 0.5$). After a further 20 iterations, the tap weights are updated by compensating the measured errors with a smaller update factor ($\mu_{MZI} = \mu_{PS} = 0.3$).

Fig. 6 shows that the frequency response of the 4-tap signal processing core after the training process, by characterizing with
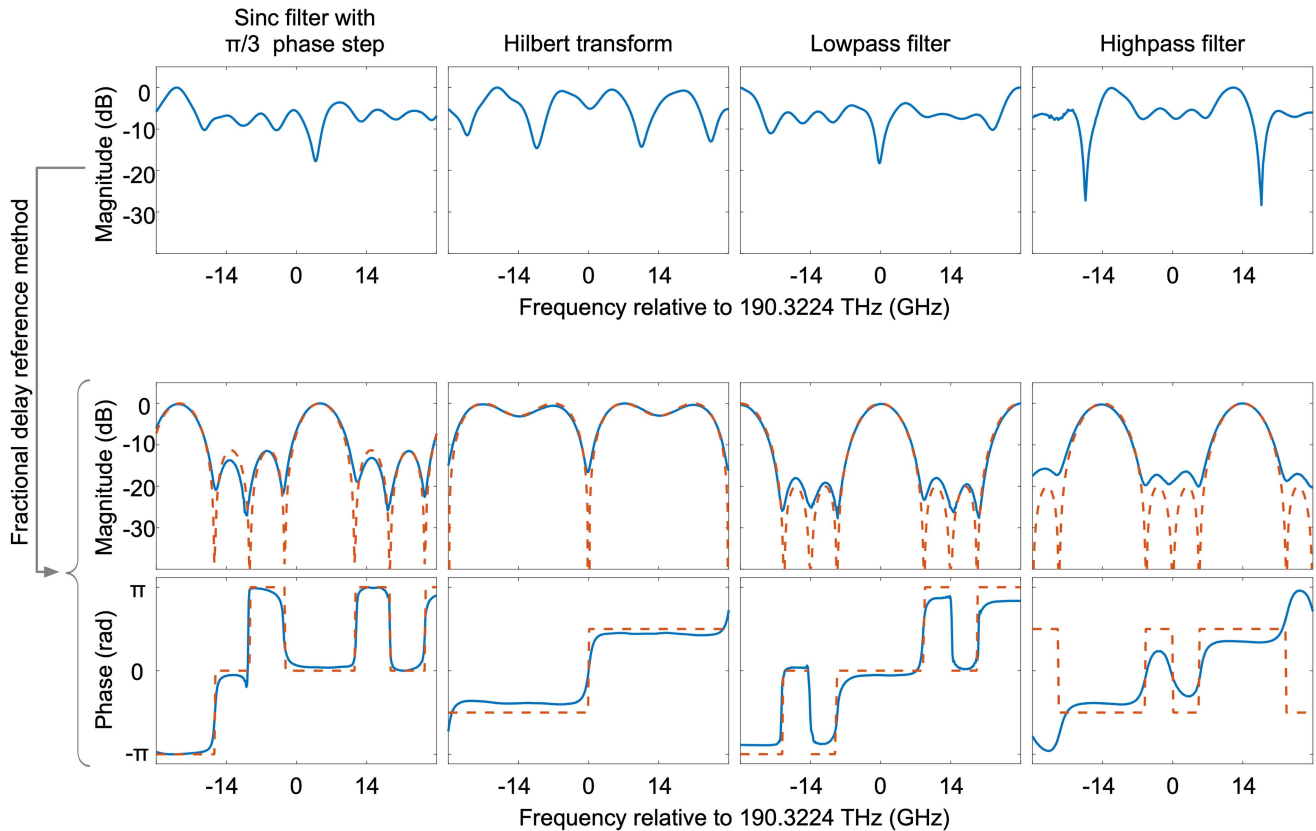
Fig. 6.   Converged frequency responses of the training circuit and the signal processing core after self-tuning for various signal-processing functions.

using Signal In and Signal Out as the optical I/O. The signal processing core is successfully self-tuned to perform the desired functions within two FSRs. We note that the phase differences exist away from the main peaks of the response, which may be due to phase being difficult to determine when the power is low. The frequency resolution of the phase measurements will also smooth the measured response. We also note that a 4-tap FIR filter is limited in the types of response it can provide and the sharpness of the responses due to the simple architecture. However, we anticipate that our control techniques can be used for a more-complex signal processing core or for a wider diversity of processing functions.

Our method essentially finds the impulse response of a filter. For Linear Time-Invariant (LTI) systems, the system is completely characterized by the impulse response; however, this does not generally mean that the coefficients within the system can be simply related from the impulse response, though obviously there are many methods to determine what the design coefficients should be from the desired impulse response. The FIR filter is a simple case where each peak in the impulse response directly relates to a tap weight. Thus, we can directly determine the amplitudes and phases of each tap, as each tap corresponds to the output of the inverse Fourier Transform at different delays. For infinite impulse response (IIR) filters, one filter coefficient (such as the coupling to a ring resonator) will appear at many outputs of the FT (separated by the round-trip delay of the resonator), but there is still the possibility of relating

the rate of decay to the coupling factor, to enable adjustment. For multiple IIR resonators [31], some overlaps may occur, particularly if the resonators have delays that are multiples of a base delay. Thus, there is a more-complex mapping of delay to a particular design coefficient; but again method exist to determine these relationships (for example, an iterative method could identify the contribution of the longest-delay resonator, then subtract it from the response, allowing the next-longest resonator to be identified). For highly-meshed networks with multiple paths across the network that all have the same delay [32], [33], it would be more difficult to uniquely relate each peak in the impulse response to a single coupling coefficient in the mesh. However, it may not be necessary to do this, as the design goal could be reached by any of many possible combinations of coupling coefficients. This is an area for further research.

VIII. CONCLUSION

In this contribution, we introduced a 'dial-up' PIC filter for the first time, which employs the fractional delay reference method within a feedback system to individually determine the tap weights of the FIR filter. We have demonstrated the method using a Si_3N_4/LNOI platform, comprising a 4-tap FIR filter and an on-chip half-delay reference path. Our experimental results show that despite thermal crosstalk the tunable components of the signal processing core can be calibrated by the algorithm with a 3%-variance of MZI's electrical power required for

2π-phase shift, and the 4-tap filter can be successfully self-tuned to perform different signal processing functions by recovering individual tap weights and controlling each tap respectively. Our demonstration of the 'dial-up' PIC filter provides the potential for a wide adoption of programmable PICs with performing various signal processing functions accurately.

REFERENCES

[1] F. Kish et al., "System-on-chip photonic integrated circuits," *IEEE J. Sel. Topics Quantum Electron.*, vol. 24, no. 1, pp. 1–20, Jan./Feb. 2018.

[2] Y. Xie, L. Zhuang, and A. J. Lowery, "Picosecond optical pulse processing using a terahertz-bandwidth reconfigurable photonic integrated circuit," *Nanophotonics*, vol. 7, no. 5, pp. 837–852, 2018.

[3] N. C. Harris et al., "Large-scale quantum photonic circuits in silicon," *Nanophotonics*, vol. 5, no. 3, pp. 456–468, 2016.

[4] J. Notaros et al., "Programmable dispersion on a photonic integrated circuit for classical and quantum applications," *Opt. Exp.*, vol. 25, no. 18, pp. 21275–21285, 2017.

[5] T. F. De Lima, B. J. Shastri, A. N. Tait, M. A. Nahmias, and P. R. Prucnal, "Progress in neuromorphic photonics," *Nanophotonics*, vol. 6, no. 3, pp. 577–599, 2017.

[6] H.-T. Peng, M. A. Nahmias, T. F. De Lima, A. N. Tait, and B. J. Shastri, "Neuromorphic photonic integrated circuits," *IEEE J. Sel. Topics Quantum Electron.*, vol. 24, no. 6, pp. 1–15, Nov./Dec. 2018.

[7] B. J. Shastri et al., "Photonics for artificial intelligence and neuromorphic computing," *Nature Photon.*, vol. 15, no. 2, pp. 102–114, 2021.

[8] Y. Shen et al., "Deep learning with coherent nanophotonic circuits," *Nature Photon.*, vol. 11, no. 7, pp. 441–446, 2017.

[9] N. C. Harris et al., "Linear programmable nanophotonic processors," *Optica*, vol. 5, no. 12, pp. 1623–1631, 2018.

[10] N. Einspruch, *Application Specific Integrated Circuit (ASIC) Technology*, vol. 23. Cambridge, MA, USA: Academic Press, 2012.

[11] S. Stopmski et al., "Application specific photonic integrated circuits for telecommunications," in *Proc. IEEE Conf. Lasers Electro- Opt. Europe Int. Quantum Electron. Conf.*, 2013, pp. 1–1.

[12] P. Nayak, "A study of technology roadmap for application-specific integrated circuit," Ph.D. dissertation, Elect. Comput. Eng. Dept., Rice Univ., Houston, TX, USA, 2021.

[13] J. Capmany and D. Pérez, *Programmable Integrated Photonics*. Oxford, U.K.: Oxford Univ. Press, 2020.

[14] W. Bogaerts et al., "Programmable photonic circuits," *Nature*, vol. 586, no. 7828, pp. 207–216, 2020.

[15] X. Chen et al., "The emergence of silicon photonics as a flexible technology platform," *Proc. IEEE*, vol. 106, no. 12, pp. 2101–2116, Dec. 2018.

[16] A. Boes, B. Corcoran, L. Chang, J. Bowers, and A. Mitchell, "Status and potential of lithium niobate on insulator (lnoi) for photonic integrated circuits," *Laser Photon. Rev.*, vol. 12, no. 4, 2018, Art. no. 1700256.

[17] L. M. Augustin et al., "InP-based generic foundry platform for photonic integrated circuits," *IEEE J. Sel. Topics Quantum Electron.*, vol. 24, no. 1, pp. 1–10, Jan./Feb. 2018.

[18] M. Jacques, A. Samani, E. El-Fiky, D. Patel, Z. Xing, and D. V. Plant, "Optimization of thermo-optic phase-shifter design and mitigation of thermal crosstalk on the SOI platform," *Opt. Exp.*, vol. 27, no. 8, pp. 10456–10471, 2019.

[19] M. Milanizadeh, D. Aguiar, A. Melloni, and F. Morichetti, "Canceling thermal cross-talk effects in photonic integrated circuits," *J. Lightw. Technol.*, vol. 37, no. 4, pp. 1325–1332, Feb. 2019.

[20] X. Liu, and A. J. Lowery, "Optical adaptive LMS equalizer with an optoelectronic feedback loop," in *Conf. Lasers and Electro-Optics*, Optical Publishing Group, San Jose, CA, USA, 2022, paper SM3J-3.

[21] D. A. Miller, "Self-configuring universal linear optical component," *Photon. Res.*, vol. 1, no. 1, pp. 1–15, 2013.

[22] D. A. Miller, "Perfect optics with imperfect components," *Optica*, vol. 2, no. 8, pp. 747–750, 2015.

[23] A. Ribeiro, A. Ruocco, L. Vanacker, and W. Bogaerts, "Demonstration of a 4×4-port universal linear circuit," *Optica*, vol. 3, no. 12, pp. 1348–1357, 2016.

[24] D. P. López, "Programmable integrated silicon photonics waveguide meshes: Optimized designs and control algorithms," *IEEE J. Sel. Topics Quantum Electron.*, vol. 26, no. 2, pp. 1–12, Mar./Apr. 2020.

[25] X. Xu et al., "Self-calibrating programmable photonic integrated circuits," *Nature Photon.*, vol. 16, no. 8, pp. 595–602, 2022.

[26] X. Xu et al., "Phase retrieval of programmable photonic integrated circuits based on an on-chip fractional-delay reference path," *Optica*, vol. 9, no. 12, 2022.

[27] J. Armstrong and A. J. Lowery, "Power efficient optical OFDM," *Electron. Lett.*, vol. 42, no. 6, pp. 370–372, 2006.

[28] X. Han et al., "Single-step etched grating couplers for silicon nitride loaded lithium niobate on insulator platform," *Apl Photon.*, vol. 6, no. 8, 2021, Art. no. 0 86108.

[29] X. Han et al., "Mode and polarization-division multiplexing based on silicon nitride loaded lithium niobate on insulator platform," *Laser Photon. Rev.*, vol. 16, no. 1, 2022, Art. no. 2100529.

[30] L. Carroll et al., "Photonic packaging: Transforming silicon photonic integrated circuits into photonic devices," *Appl. Sci.*, vol. 6, no. 12, 2016, Art. no. 426.

[31] T. F. de Lima et al., "Design automation of photonic resonator weights," *Nanophotonics*, vol. 11, pp. 3805–3822, 2022.

[32] D. Pérez-López, A. López, P. DasMahapatra, and J. Capmany, "Multipurpose self-configuration of programmable photonic circuits," *Nature Commun.*, vol. 11, no. 1, pp. 1–11, 2020.

[33] H. Zhang et al., "An optical neural chip for implementing complex-valued neural network," *Nature Commun.*, vol. 12, no. 1, pp. 1–11, 2021.